

# Tunable Metasurface Inverse Design for 80% Switching Efficiencies and 144° Angular Deflection

Haejun Chung\* and Owen D. Miller\*

Cite This: *ACS Photonics* 2020, 7, 2236–2243

Read Online

ACCESS |



Metrics &amp; More



Article Recommendations

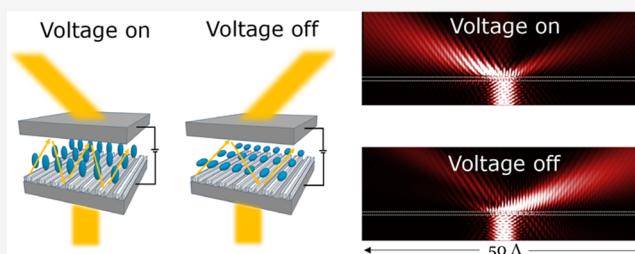


Supporting Information

**ABSTRACT:** Tunable metasurfaces have demonstrated the potential for dramatically enhanced functionality for applications including sensing, ranging and imaging. Liquid crystals (LCs) have fast switching speeds, low cost, and mature technological development, offering a versatile platform for electrical tunability. However, to date, electrically tunable metasurfaces are typically designed at a single operational state using physical intuition, without controlling alternate states and thus leading to limited switching efficiencies (<30%) and small angular deflection (<25°). Here, we use large-scale computational “inverse design” to discover high-performance designs through adjoint-based local-optimization design iterations within a global-optimization search. We study and explain the physics of these devices, which heavily rely on sophisticated resonator design to fully utilize the very small permittivity change incurred by switching the liquid-crystal voltage. The optimal devices show tunable deflection angles ranging from 12° to 144° and switching efficiencies above 80%, exhibiting 6× angular improvements and 6× efficiency improvements compared to the current state-of-the-art.

**KEYWORDS:** tunable metasurface, inverse design, beam deflection, liquid crystal

Liquid-crystal (LC) devices promise the possibility for rapid electrical deflection of optical beams, yet the complexity of designing for multiple refractive-index states in a single geometry has severely restricted the resulting diffraction efficiencies (<50%), switching efficiencies (defined below, <25%), and deflection angles ( $\leq 24^\circ$ ), even in state-of-the-art designs.<sup>1</sup> In this work, we show that large-scale computational optimization, “inverse design,” is particularly well-suited to harnessing structural complexity to achieve high multistate efficiencies in tunable devices, where intuition-based approaches falter. We discover fabrication-ready designs with switching efficiencies and diffraction efficiencies above 80% and deflection angles up to 144°. We combine adjoint-based gradients<sup>2–9</sup> for rapid local optimization within a larger global search to discover the high-efficiency (>80%) and high-deflection-angle designs (144°). We compute the complex resonance patterns of the optimal devices, which reveal several competing design requirements that explain the need for computational optimization of many degrees of freedom. Unlike metasurfaces designed for lens-like focusing<sup>10–17</sup> and related applications,<sup>18–21</sup> we find that the optimal devices should have their field intensities concentrated not in the high-index grating material, but instead, in the low-index liquid-crystal embedding medium, to enable high switching efficiencies even for the relatively small refractive-index changes of LCs. Our largest-deflection-angle devices exhibit 90% diffraction efficiency at  $-72^\circ$  in the off state and 70% diffraction efficiency at  $+72^\circ$  in the on state, simultaneously exhibiting 6× angular and almost 6×

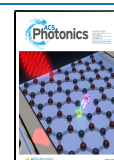


switching-efficiency enhancements over the current state-of-the-art, paving a pathway to efficient liquid-crystal beam-control devices for applications ranging from LiDAR<sup>22,23</sup> to spatial light modulator.<sup>24</sup>

Thin optical films with complex lithographic patterns can control phases, amplitudes, diffraction-order excitations, and more general wave dynamics with high efficiency over large-area devices, comprising the basis for the emerging field of metasurfaces.<sup>10,25</sup> Metasurfaces have shown significant promise for static (nontunable) applications such as holography,<sup>18–20</sup> lensing,<sup>10–17</sup> and beam converters,<sup>26,27</sup> in large part due to the use of a relatively simple design principle: for a given frequency of interest, one can specify the desired outgoing phases and amplitudes (and possibly dispersion characteristics<sup>25</sup>) across the device surface and select from a library of waveguide-like meta-elements to locally approximate those phases and amplitudes. This design principle is not exact, the local-periodicity assumption is a source of error, especially in high-NA lens applications,<sup>28,29</sup> and there is significant effort to leverage

Received: May 12, 2020

Published: July 28, 2020



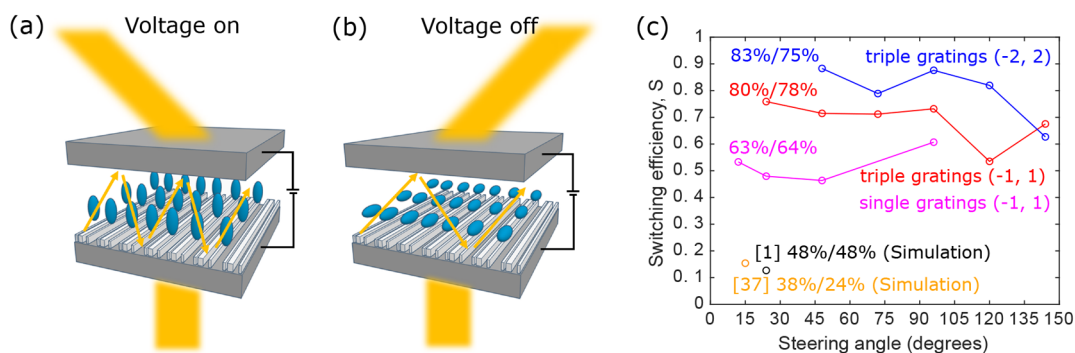


**Figure 1.** Tunable metasurface via inverse design. (a) In the voltage-on state, the LC director is aligned along the vertical direction, perpendicular to TE-mode electric fields. A designed grating ideally deflects incident light to the target angle. (b) When the voltage is off, the LC director is now parallel to TE-mode electric fields, thus, maximizing the effective refractive-index change of the LC, as seen by the fields. (c) Switching efficiency of our designed devices and existing devices over a wide range of deflection angles. The efficiencies denoted within the figure (e.g., 83%/75%) represent the highest diffraction efficiencies of each type of device in the on/off states. Switching efficiency, defined in eq 1, measures the distinguishability of the two operational states. The optimal devices show tunable deflection angles ranging from 12° to 144°, offering 6× angular increase with the 144° deflection metasurface and 6× switching-efficiency improvement with the 96° deflection metasurface compared to the current state-of-the-art.<sup>1</sup> Note that all comparisons we make are to theoretical designs.

computation to improve it,<sup>29–31</sup> but it has been sufficient for proof-of-principle high-performance devices.

For dynamic applications, however, in which the properties of the metasurface are designed to offer varying functionality in multiple operational states, from electrical,<sup>32–35</sup> mechanical,<sup>36</sup> or thermal<sup>37</sup> switching mechanisms, the simple design principle appears to be quite inefficient. One might imagine that multistate operation would require only small extra considerations in the “library” of designs, accounting for the additional states. However, as we show below, the requirement for high-efficiency resonant behavior in multiple states rapidly leads to highly complex resonant patterns, with individual elements far more complex than those of typical metasurface applications, due to the requirement for the multistate behavior to be supported by a single geometrical structure. In lieu of a multistate design principle, previous approaches<sup>33,38–40</sup> have simplified the design process by focusing only on high efficiency for a single state, but this naturally leads to lower efficiencies in the switching process over the dynamic range of the devices. (An alternative approach is to use a frequency comb in tandem with a designed metasurface, which can create time-dependent beam profiles albeit without full temporal steering control.<sup>41</sup>)

In this work, we show that large-scale computational design, an approach that efficiently optimizes over arbitrarily many degrees of freedom, offers a pathway to high-efficiency dynamic (tunable) metasurfaces. We focus on beam-switching with liquid-crystal devices, which already have significant commercial development and which show promise for applications such as LiDAR. We discuss the complexity of the design space, and describe a combined application of adjoint-based local-optimization techniques within a larger global-optimization platform, and use this approach to discover two-state switching devices with high switching efficiencies and high deflection angles.

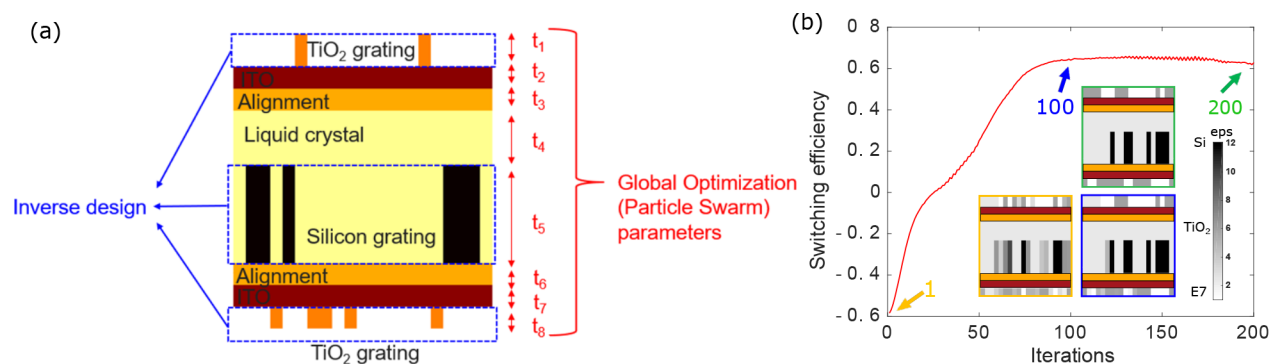
## ■ COMPUTATIONAL MULTISTATE DESIGN

Figure 1a,b is a schematic depiction of a liquid-crystal (LC) beam-switching device. As is typical in LC devices,<sup>40,42</sup> the liquid-crystal layer is embedded between two alignment and contact layers. Within the LC region, and above and below the contact layers, complex patterns can be lithographically

fabricated, and previous work has designed grating layers for moderate-efficiency electrical<sup>1,40,43</sup> and thermal<sup>37</sup> switching of LC devices. The key metric to design for is the switching efficiency, that is, how effectively the device can switch between different optical-beam patterns. For periodic grating and meta-grating structures, diffraction efficiency is an important determinant of the switching efficiency, but not the only one: a device that separates an optical field into a 50% mix of two outgoing diffraction orders, for both voltages of a two-state device, effectively has zero switching efficiency due to the inability to distinguish the two states. Moreover, in many cases, back-reflected light represents only a minor loss mechanism, without affecting the relative power distribution between the forward-going beams nor the ability to distinguish them and can be normalized out. Thus, for a two-state optical-switching device operating over frequencies  $\omega$  with geometrical degrees of freedom  $g$ , we define switching efficiency by the expression

$$S = \frac{1}{T} \left\{ \frac{1}{2} \sum_{s=\text{on,off}} \left[ P_{\text{tar}}^s(\omega, g) - \sum_{j \neq \text{tar}} P_j^s(\omega, g) \right] \right\} \quad (1)$$

which is the power in the target (desired) diffraction orders,  $P_{\text{tar}}^s(\omega, g)$ , averaged over state  $s$ , minus the total state-averaged power in all other diffraction orders,  $P_{j \neq \text{tar}}^s(\omega, g)$ , normalized by the forward transmission efficiency  $T$ . This definition of switching efficiency, which can be easily generalized to more states, linear combinations of diffraction orders, and so on, enables a comparison among different device designs. Figure 1c shows the switching efficiencies of recent state-of-the-art LC beam-switching devices, which show moderate diffraction efficiencies (24–54%, labeled), but somewhat lower switching efficiencies (ranging from 13% to 29%), due to the contamination of unwanted diffraction orders that inhibit the ability to distinguish the on/off states. Included in Figure 1c are the switching efficiencies of the optimal devices that we discover, discussed further below, segregated into three architectures: a class of devices with a single silicon grating in the liquid-crystal region (solid purple line) and two classes of devices with two additional gratings on the top and bottom, one for  $-1$  to  $+1$  order deflection (solid red line) and one for  $-2$  to  $+2$  order deflection (solid blue line). There are many geometrical degrees



**Figure 2.** Design framework. (a) Schematic diagram showing a combined strategy of global search and local inverse design. Every agent and every iteration of the global search performs a complete inverse design procedure with different layer thicknesses. (b) Switching efficiency over inverse design iterations. Yellow, blue, and green inset figures indicate 1, 100, and 200th iteration, respectively. The switching efficiency increases over the early stage of the iterations, then the grayscale structure becomes binary as penalization kicks in.

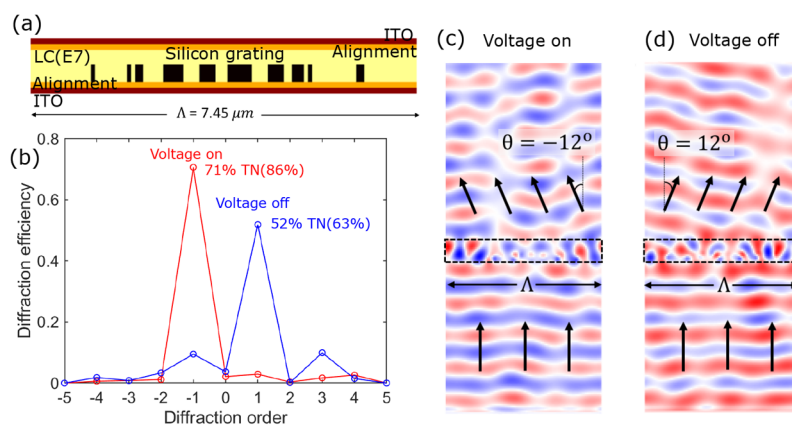


**Figure 3.** Optimization of a single-grating tunable metasurface via inverse design at 1550 nm wavelength. (a) Optimized structure showing silicon grating inside the LC layer (E7). The period of the structure is  $4.8\lambda$  long ( $7.44 \mu\text{m}$ ). The LC region and silicon grating have thicknesses of 697.5 and 387.5 nm, respectively. The ITO and alignment layers have 77.5 nm thickness. (b) Diffraction efficiency of the optimized device at 1550 nm wavelength. The unwanted order diffractions are suppressed well via the FOM defined in this work, maintaining high efficiencies in the target orders. (c, d) Real parts of the electric field for the (c) voltage-on and (d) voltage-off states. They show clear outgoing fields propagating toward  $\pm 12^\circ$ .

of freedom in each architecture: the individual “pixels” (77.5 nm wide) of each grating, the thicknesses of the alignment, contact, and LC layers, and the period of the structure. The pixel size is chosen as  $\lambda/20$  to provide sufficient control while avoiding features that are too fine for fabrication. We take the switching to occur between two states with the same polarization, in which case the gratings can be chosen to have translation invariance perpendicular to a plane containing both angles, and the system can be modeled in this two-dimensional plane. There are many grating degrees of freedom ( $\approx 400$ ), and to optimize these, it is critical to be able to rapidly compute gradients of the switching-efficiency objective. To do so, we use the adjoint method (also known as “topology optimization”<sup>2,44</sup> and “inverse design”<sup>3,4,6,7,45–54</sup> in nanophotonics and “backpropagation” in the deep-learning community<sup>55–57</sup>), which is efficient and effective at optimizing many small-scale degrees of freedom.<sup>8</sup> Adjoint-based methods exploit reciprocity (or generalized reciprocity<sup>5</sup>) to convert the process of computing thousands or millions of individual gradient calculations into a single extra simulation, in which “adjoint sources” are specified according to the desired objective, back-propagated through the optical system, and then combined with the “direct” fields excited by the original incident wave to compute all gradients at once. For an objective  $\mathcal{F}$  such as switching efficiency, eq 1, that depends on

the outgoing electric fields  $E$ , the general prescription<sup>5</sup> for each “forward” simulation (in this case, the voltage-on and voltage-off simulations) is to run an “adjoint” simulation with current sources proportional to the derivative of the objective with respect to the electric field (SM):

$$\begin{aligned} \mathbf{J}_{\text{adj}}(\mathbf{x}) &= -i\omega \frac{\partial \mathcal{F}}{\partial \mathbf{E}} \\ &= -\frac{i\omega}{2} \left[ c_{\text{tar}} \cos \theta_{\text{tar}} \mathbf{E}_{\text{tar}}^*(\mathbf{x}) - \sum_{n \neq \text{tar}} c_n \cos \theta_n \mathbf{E}_n^*(\mathbf{x}) \right] \end{aligned} \quad (2)$$

In our adjoint equation indicated by eq 2, we exclude the  $1/T$  of eq 1 to drive the optimization to exhibit high transmission in addition to high switching efficiency. The pixels in the gratings are represented during the design process as grayscale pixels, with refractive indices varying between their minimum and maximum values, and as the local optimization proceeds, we penalize intermediate refractive-index values until a binary design is reached. This process is very efficient for the many grating degrees of freedom. However, it is less efficient for variables representing larger geometrical parameters: the thicknesses of the various regions and the periodicity of the structure. Wave-interference effects create a tremendous number of poor-quality, local optima for these parameters,

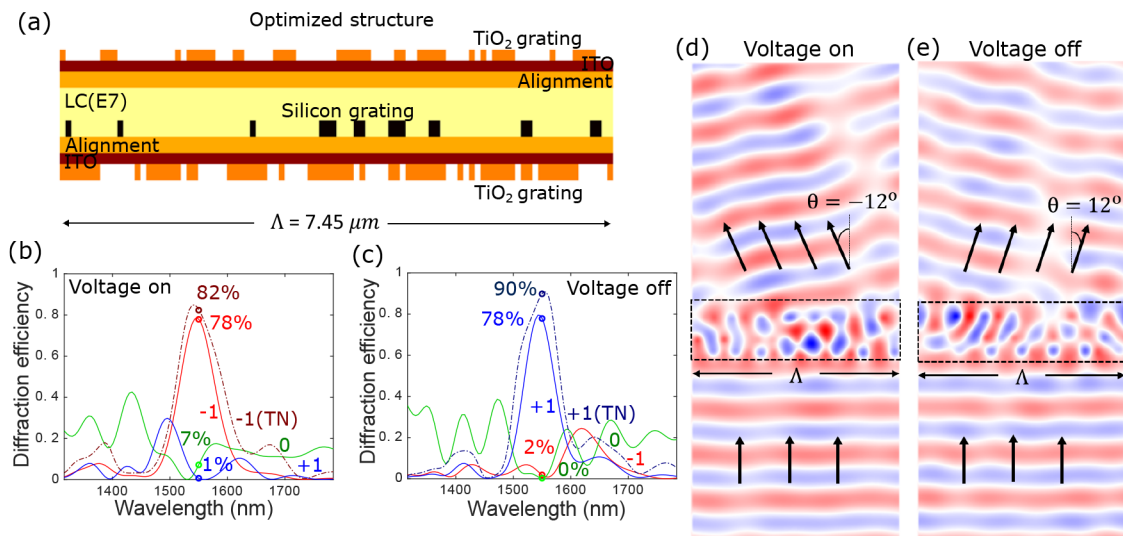


**Figure 4.** Optimized triple-grating tunable metasurface for narrow-angle ( $\pm 12^\circ$ ) deflection with high efficiency. (a) Optimized structure showing triple gratings ( $\text{TiO}_2/\text{Si}/\text{TiO}_2$ ). The period of the structure is  $4.8\lambda$  ( $7.44 \mu\text{m}$ ) and the thicknesses of the LC, silicon grating, top  $\text{TiO}_2$  and bottom  $\text{TiO}_2$  are 542.5, 155, 155, and 232.5 nm, respectively. The ITO is 77.5 nm thick, and the alignment layer is 155 nm thick. (b, c) Diffraction efficiencies over infrared wavelengths for the (b) voltage-on and (c) voltage-off states. “TN” denotes transmission normalized efficiency. The optimized grating shows  $-1$  order efficiency of 78% in the voltage-on state and  $+1$  order efficiency of 78% in the voltage-off state. The transmission-normalized efficiencies are 82% and 90%, respectively. (d, e) Real parts of the electric fields for the (d) voltage-on and (e) voltage-off states.

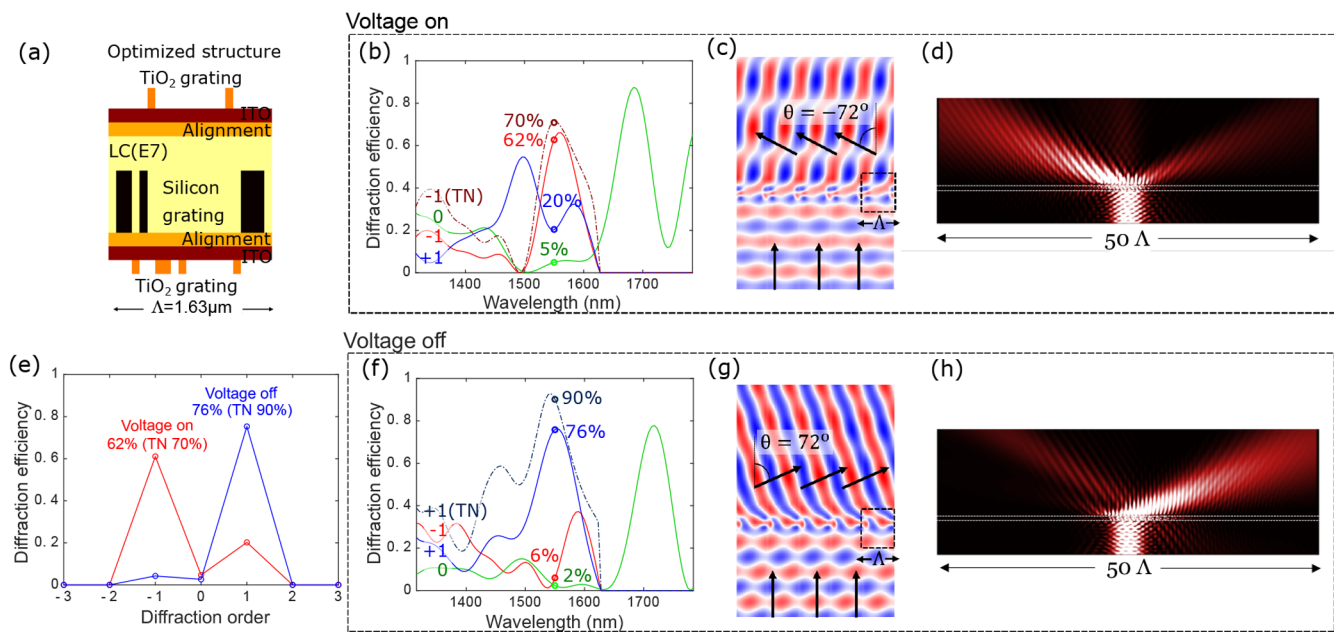


**Figure 5.** Optimized triple-grating tunable metasurface for ultrawide-angle ( $\pm 72^\circ$ ) deflection. (a) Optimized structure showing triple gratings ( $\text{TiO}_2/\text{Si}/\text{TiO}_2$ ). The period of the structure is  $1.05\lambda$  ( $1.628 \mu\text{m}$ ) and the thicknesses of the LC, silicon grating, top  $\text{TiO}_2$ , and bottom  $\text{TiO}_2$  are 930, 620, 232.5, and 155 nm, respectively. The ITO and the alignment layer both have 77 nm thicknesses. (b, f) Diffraction efficiencies over the infrared spectrum for the (b) voltage-on and (f) voltage-off states. TN means transmission normalized efficiency. The optimized grating shows  $-1$  order diffraction efficiency of 62% in the voltage-on state and  $+1$  order efficiency of 76% in the voltage-off state. The transmission-normalized efficiencies are 70% and 90%, respectively. (c, g) Real parts of the electric fields for the (c) voltage-on and (g) voltage-off states. (d, h) E-field intensity profile at 1550 nm wavelength for a supercell with an array of 50 unit cells excited by a Gaussian beam of  $5\lambda$  width centered at 1550 nm wavelength. The white dashed lines indicate the areas of the supercells.

since varying them even by half a wavelength or less can take one from a field minimum to a maximum.

The many-local-optima problems for these “global” (beyond wavelength-scale) parameters could be significantly compensated by separating them into pixelated local degrees of freedom (DOFs) that vary independently. However, they are fixed by fabrication constraints and must not be separated. Thus, to

optimize these parameters, we embedded the grating-DOF local-optimization procedure into a global search to discover optimal thickness and periodicity values, as shown in Figure 2. Particle swarm optimization<sup>58</sup> is used for a global optimization algorithm, initially instantiating many “particles” with random structural parameters (i.e., top  $\text{TiO}_2$  grating, ITO, alignment, LC, silicon grating and bottom  $\text{TiO}_2$  grating thicknesses).

Within each “particle”, we perform inverse design, computed in a single computational core, optimizing the fine-scale features of the device. Then, new parameters are chosen based on the evaluation function of the standard Particle Swarm Optimization (PSO).<sup>59</sup> eq 1 is used for the evaluation function while layer thicknesses are the parameters to be optimized. Without the global search, our single-grating designs showed only 37% switching efficiency with dozens of local searches, versus 53% switching efficiency with a global search. The global optimization is run for 150 iterations, which is sufficient to converge to a set of very similar “particles,” with similar large-scale-feature values. Each iteration of global optimization takes approximately 10 min on 25 cores in our computational cluster (Intel Xeon E5–2660 v4 3.2 GHz processors), while each inverse design iteration takes less than 5 s in a single core computer.

## ■ OPTIMAL DESIGNS

We apply the multistate computational design process described above to discover the single- and multigrating designs depicted in Figures 3–5. We start by designing LC metasurfaces with a single embedded silicon grating, intentionally selecting a platform very similar to that of recent works<sup>1,37</sup> to show the efficiency gains that are possible through computational design. Then we expand to structures with multiple grating layers, where we show the extensive capability for LC metasurfaces to simultaneously achieve high efficiency and high deflection angles. In all of the designs demonstrated below, we use 1550 nm as our design wavelength. For the LC material, we use E7,<sup>60</sup> which has a refractive-index variation  $\Delta n$  of about 0.192 between the voltage-on and voltage-off states. TiO<sub>2</sub><sup>61</sup> is used for top and bottom supportive gratings, while we use silicon for the grating inside the LC layer. ITO<sup>62</sup> and alignment layers<sup>37,42,63</sup> are included, as typically required. Unlike metasurfaces for lensing and related applications, high-index materials do not appear to be required for high diffraction efficiency nor switching efficiency; we use Si and TiO<sub>2</sub> simply because of their common usage<sup>1,37,40</sup> and scale-up feasibility. The top ITO works as an electrical contact, and the alignment layer coordinates the axis of the LC director into the out-of-plane direction. Of course, a different wavelength, set of materials, or parameter regime can seamlessly be incorporated into our design process.

**Single-Grating Designs.** In this section, we design tunable metasurfaces with a single grating layer. Single-grating metasurfaces can be designed by physical intuition using effective medium theory,<sup>64</sup> whereby the filling ratio of two materials is adjusted to realize specific transmission phases or by a unit-cell library approach,<sup>10</sup> whereby a large design space is decomposed into “unit cells” with a small number of parameters whose entire design space can be stored in a library to design for a small number of criteria. Neither approach is well-suited to designing many parameters for multistate operation.

Figure 3 shows an optimal single-grating design for switching between  $-12^\circ$  and  $+12^\circ$ , angles chosen to match the current state-of-the-art.<sup>1</sup> The optimized single-grating metasurface achieves diffraction efficiencies of 71% in the voltage-on state and 52% in the voltage-off state, with clean outgoing field patterns visible in Figure 3c,d. A key determinant of the angular purity is the diffraction efficiency normalized by the total transmission, since reflection does not contribute noise in the outgoing-wave patterns, and the transmission-normalized (TN) efficiencies of these structures are 86% and 63%, respectively. During the optimization, we fix the top and bottom sides to have

thin ITO and alignment layers, while we include the thicknesses of the LC layer and the silicon grating as global design parameters. The beam switching efficiency (48%) shown here is already significantly larger than any other theoretical designs. However, for key applications, one can expect the need for larger deflection angles and even high switching efficiencies. Thus, in the next section, we explore more complex device architectures.

**Multigrating Designs.** In this section, we design tunable metasurfaces with three gratings, one in the silicon and two in the TiO<sub>2</sub> surroundings, to discover an ultrahigh-efficiency, beam-switching device. Generally, multilayer metasurface structures offer increased functionality through increased path-length enhancements and multiple-reflection interactions, and multilayer metasurfaces have been proposed for light concentration<sup>29</sup> and flat lens<sup>9</sup> applications. Here, the two TiO<sub>2</sub> gratings must enable specific functionality: the bottom grating must be transmissive for the plane-wave incident from below while being highly reflective for all off-angle plane waves reflected from above, and the top grating should either redirect all light to the single desired outgoing diffraction order or at least restrict transmission through any undesired orders. Though the use of multiple gratings requires precise alignment, the gratings play complementary roles and potentially enable near-unity switching efficiencies even at very high switching angles.

We start by reconsidering the problem of high-efficiency switching from  $-12^\circ$  to  $+12^\circ$ . The optimal design, depicted in Figure 4a, achieves diffraction efficiencies of 78% (82% TN) in the voltage-on state and 78% (90% TN) in the voltage-off state, for a switching efficiency of 76%, with very little power in any other outgoing diffraction orders. The clean outgoing waves are depicted in Figure 4d,e. The optimized device has ITO/alignment layer thicknesses of 77.5 and 155 nm, top and bottom grating thicknesses of 155 and 232.5 nm, a silicon grating thickness of 155 nm, and a liquid-crystal layer thickness of 542.5 nm.

Among the many designs that were discovered across the single-, double-, and triple-grating architectures, for beam-deflection angles from  $24^\circ$  to  $144^\circ$ , we highlight here the highest deflection-angle designs, which employ a triple-grating structure to achieve deflection from  $-72^\circ$  to  $+72^\circ$ . By avoiding a design with collections of locally varying “unit cells,” we circumvent the limitations<sup>28</sup> arising from breaking the local-periodicity assumption. Figure 5 shows an optimal structure with thickness  $1.628 \mu\text{m}$  and period  $1.628 \mu\text{m}$  (which is  $1.05\lambda$ ). The diffraction efficiencies in the target orders are 62% and 76% for voltage-on and -off states, respectively, while the transmission normalized target efficiencies are 70% and 90%, respectively. These diffraction efficiencies are individually nearly as large as those of state-of-the-art high-angle diffraction gratings that are designed only for a single operational state.<sup>47</sup> The real part of the electric-field profile shown in Figure 5c,g demonstrates the clear angle-directed outgoing wave patterns, and in Figure 5d,h, we simulate a Gaussian beam incident upon the structure to more clearly visualize the high-fidelity switching that is achieved. The robustness and convergence studies of this design approach are attached in the Supporting Information, where we provide information regarding a misalignment tolerance, sensitivity against fabrication error, a quantitative look at the feature and gap sizes, and convergence study. We use an assumption of infinite size in the out-of-plane direction in this study. We can expect that as long as the thickness in the out-of-plane direction is more than a few wavelengths thick, that our analysis will hold for the bulk of the device. Any implementation will necessarily

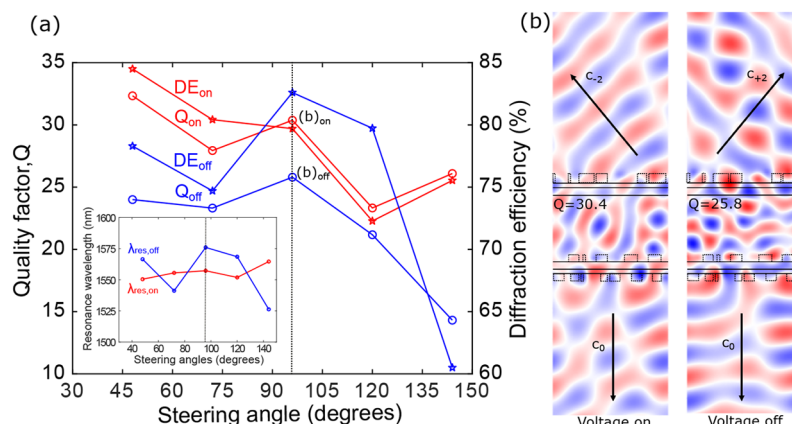


**Figure 6.** Resonance analysis of the beam-deflection metasurfaces (a) Quality factor and diffraction efficiency versus deflection angle for the triple-grating metasurfaces ( $-2$  to  $+2$ ). There is a strong correlation between the quality factors of the devices (circles) and their diffraction efficiencies (stars). The inset figure shows the resonance wavelengths of the major resonance patterns found in the optimum devices. (b) Real parts of the electric fields at their resonant frequencies ( $1571$  nm for the voltage-on state and  $1550$  nm for the voltage-off state) for  $96^\circ$  deflection angle [black dashed lines in (a)]. Quality factors found in this structure are  $30.4$  (on) and  $25.8$  (off) and the resonances strongly couple to the incident and target channels.

be many wavelengths long in the third dimension, so the errors should be miniscule from such an approximation.

To understand the physics of the high-efficiency designs that we discover, we analyze the quality factors ( $Q$ ) and resonance patterns for our high-efficiency structures designed for  $-2$  to  $+2$  order switching. As shown in Figure 6a, we find that the optimal designs are a new kind of *dual-resonance* structure that support one moderate- $Q$  resonance in the on state (red circles), and a different moderate- $Q$  resonance in the off-state (blue circles). In Figure 6b, we depict the resonant field pattern of our  $96^\circ$  deflection device, which has  $87\%$  switching efficiency and transmission-normalized efficiencies of  $86\%$  (voltage-on) and  $95\%$  (voltage-off). The field pattern is computed by exciting point dipoles at the high-intensity locations of the plane-wave forward simulation, discovering the mode responsible for the high efficiency. The resonance pattern of the voltage-on state shows strong coupling to  $c_{-2}$  channel in transmission direction and  $c_0$  channel in incidence direction, agreeing well with what one would expect. In the voltage-off state, the new resonant pattern couples to the  $c_{+2}$  channel in transmission direction and  $c_0$  channel in incidence direction. An intriguing trend in Figure 6a is that when we overlay the diffraction efficiencies (red and blue stars) with the quality factors, we observe a correlation between the two. This suggests that quality factors of at least  $30$  or so may be necessary to achieve the highest possible diffraction efficiencies in each operational state of a beam-switching or beam-deflection device.

## EXTENSIONS

In this work, we have demonstrated high-efficiency, wide-angle, electrically tunable metasurfaces that operate at  $1550$  nm wavelength, achieving state-of-the-art deflection angles and switching efficiencies. Our inverse-design approach can be applied more broadly to any multiconfiguration-state optical functionality, for applications including next-generation LiDAR, spatial light modulators, and free-space data communication. In the liquid-crystal beam-steering design space, natural extensions include many-state operation (toward steering rather than switching) and three-dimensional beam control. In addition to the “bottom-up” large-scale optimization approach presented here, an interesting question is the limits of such design: for a given set of liquid-crystal and semiconductor refractive indices,

is it possible to exploit sum rules,<sup>65–69</sup> passivity and convexity,<sup>70–73</sup> and duality<sup>74</sup> to map out the limits to maximal performance as a function of the deflection angle and the number of operational states? The other interesting extension would be designing a dual-polarization grating that could be used both in receiving and transmitting sides of the LiDAR.

## ASSOCIATED CONTENT

### Supporting Information

The Supporting Information is available free of charge at <https://pubs.acs.org/doi/10.1021/acsp Photonics.0c00787>.

Optimized single and triple grating metasurfaces, inverse design framework, misalignment tolerance, robustness study, mesh convergence study, penalization function, feature size of the optimized gratings, optimization with  $\lambda/10$  feature size for a potential extension to a visible spectrum, and geometry parameters (PDF)

## AUTHOR INFORMATION

### Corresponding Authors

**Haejun Chung** – Department of Applied Physics and Energy Sciences Institute, Yale University, New Haven, Connecticut 06511, United States; [orcid.org/0000-0001-8959-237X](https://orcid.org/0000-0001-8959-237X); Email: [haejun.chung@yale.edu](mailto:haejun.chung@yale.edu)

**Owen D. Miller** – Department of Applied Physics and Energy Sciences Institute, Yale University, New Haven, Connecticut 06511, United States; [orcid.org/0000-0003-2745-2392](https://orcid.org/0000-0003-2745-2392); Email: [owen.miller@yale.edu](mailto:owen.miller@yale.edu)

Complete contact information is available at: <https://pubs.acs.org/doi/10.1021/acsp Photonics.0c00787>

### Funding

H.C. and O.D.M. were partially supported by the Air Force Office of Scientific Research under Award Number FA9550-17-1-0093.

### Notes

The authors declare no competing financial interest.

## REFERENCES

- (1) Li, S.-Q.; Xu, X.; Veetil, R. M.; Valuckas, V.; Paniagua-Domínguez, R.; Kuznetsov, A. I. Phase-only transmissive spatial light modulator based on tunable dielectric metasurface. *Science* **2019**, *364*, 1087–1090.
- (2) Bendsoe, M. P.; Sigmund, O. *Topology Optimization: Theory, Methods, And Applications*; Springer Science & Business Media, 2013.
- (3) Jensen, J. S.; Sigmund, O. Topology optimization for nanophotonics. *Laser & Photonics Reviews* **2011**, *5*, 308–321.
- (4) Yang, L.; Lavrinenko, A. V.; Hvam, J. M.; Sigmund, O. Design of one-dimensional optical pulse-shaping filters by time-domain topology optimization. *Appl. Phys. Lett.* **2009**, *95*, 261101.
- (5) Miller, O. D. Photonic Design: From Fundamental Solar Cell Physics to Computational Inverse Design. *Ph.D. Thesis*, University of California, Berkeley, 2012.
- (6) Lalau-Keraly, C. M.; Bhargava, S.; Miller, O. D.; Yablonovitch, E. Adjoint shape optimization applied to electromagnetic design. *Opt. Express* **2013**, *21*, 21693–21701.
- (7) Piggott, A. Y.; Lu, J.; Lagoudakis, K. G.; Petykiewicz, J.; Babinec, T. M.; Vučković, J. Inverse design and demonstration of a compact and broadband on-chip wavelength demultiplexer. *Nat. Photonics* **2015**, *9*, 374–377.
- (8) Molesky, S.; Lin, Z.; Piggott, A. Y.; Jin, W.; Vučković, J.; Rodriguez, A. W. Inverse design in nanophotonics. *Nat. Photonics* **2018**, *12*, 659.
- (9) Lin, Z.; Groever, B.; Capasso, F.; Rodriguez, A. W.; Lončar, M. Topology-Optimized Multilayered Metaoptics. *Phys. Rev. Appl.* **2018**, *9*, No. 044030.
- (10) Aieta, F.; Kats, M. A.; Genevet, P.; Capasso, F. Multiwavelength achromatic metasurfaces by dispersive phase compensation. *Science* **2015**, *347*, 1342–1345.
- (11) Khorasaninejad, M.; Aieta, F.; Kanhaiya, P.; Kats, M. A.; Genevet, P.; Rousso, D.; Capasso, F. Achromatic metasurface lens at telecommunication wavelengths. *Nano Lett.* **2015**, *15*, 5358–5362.
- (12) Avayu, O.; Almeida, E.; Prior, Y.; Ellenbogen, T. Composite functional metasurfaces for multispectral achromatic optics. *Nat. Commun.* **2017**, *8*, 14992.
- (13) Shrestha, S.; Overvig, A. C.; Lu, M.; Stein, A.; Yu, N. Broadband achromatic dielectric metalenses. *Light: Sci. Appl.* **2018**, *7*, 85.
- (14) Chen, B. H.; Wu, P. C.; Su, V.-C.; Lai, Y.-C.; Chu, C. H.; Lee, I. C.; Chen, J.-W.; Chen, Y. H.; Lan, Y.-C.; Kuan, C.-H.; Tsai, D. P. GaN metalens for pixel-level full-color routing at visible light. *Nano Lett.* **2017**, *17*, 6345–6352.
- (15) Paniagua-Domínguez, R.; Yu, Y. F.; Khaidarov, E.; Choi, S.; Leong, V.; Bakker, R. M.; Liang, X.; Fu, Y. H.; Valuckas, V.; Krivitsky, L. A.; Kuznetsov, A. I. A metalens with a near-unity numerical aperture. *Nano Lett.* **2018**, *18*, 2124–2132.
- (16) Chen, W. T.; Zhu, A. Y.; Sanjeev, V.; Khorasaninejad, M.; Shi, Z.; Lee, E.; Capasso, F. A broadband achromatic metalens for focusing and imaging in the visible. *Nat. Nanotechnol.* **2018**, *13*, 220.
- (17) Wang, S.; et al. A broadband achromatic metalens in the visible. *Nat. Nanotechnol.* **2018**, *13*, 227.
- (18) Zheng, G.; Mühlenernd, H.; Kenney, M.; Li, G.; Zentgraf, T.; Zhang, S. Metasurface holograms reaching 80% efficiency. *Nat. Nanotechnol.* **2015**, *10*, 308.
- (19) Ni, X.; Kildishev, A. V.; Shalae, V. M. Metasurface holograms for visible light. *Nat. Commun.* **2013**, *4*, 2807.
- (20) Zhao, W.; Liu, B.; Jiang, H.; Song, J.; Pei, Y.; Jiang, Y. Full-color hologram using spatial multiplexing of dielectric metasurface. *Opt. Lett.* **2016**, *41*, 147–150.
- (21) Arbabi, A.; Arbabi, E.; Horie, Y.; Kamali, S. M.; Faraon, A. Planar metasurface retroreflector. *Nat. Photonics* **2017**, *11*, 415.
- (22) Poulton, C. V.; Byrd, M. J.; Russo, P.; Timurdogan, E.; Khandaker, M.; Vermeulen, D.; Watts, M. R. Long-Range LiDAR and Free-Space Data Communication With High-Performance Optical Phased Arrays. *IEEE J. Sel. Top. Quantum Electron.* **2019**, *25*, 1–8.
- (23) Poulton, C. V.; Yaacobi, A.; Cole, D. B.; Byrd, M. J.; Raval, M.; Vermeulen, D.; Watts, M. R. Coherent solid-state LIDAR with silicon photonic optical phased arrays. *Opt. Lett.* **2017**, *42*, 4091–4094.
- (24) Shrestha, P. K.; Chun, Y. T.; Chu, D. A high-resolution optically addressed spatial light modulator based on ZnO nanoparticles. *Light: Sci. Appl.* **2015**, *4*, No. e259.
- (25) Yu, N.; Capasso, F. Flat optics with designer metasurfaces. *Nat. Mater.* **2014**, *13*, 139.
- (26) Wu, P. C.; Zhu, W.; Shen, Z. X.; Chong, P. H. J.; Ser, W.; Tsai, D. P.; Liu, A.-Q. Broadband Wide-Angle Multifunctional Polarization Converter via Liquid-Metal-Based Metasurface. *Adv. Opt. Mater.* **2017**, *5*, 1600938.
- (27) Chong, K. E.; Staude, I.; James, A.; Dominguez, J.; Liu, S.; Campione, S.; Subramania, G. S.; Luk, T. S.; Decker, M.; Neshev, D. N.; et al. Polarization-independent silicon metadevices for efficient optical wavefront control. *Nano Lett.* **2015**, *15*, 5369–5374.
- (28) Chung, H.; Miller, O. D. High-NA achromatic metalenses by inverse design. *Opt. Express* **2020**, *28*, 6945–6965.
- (29) Lin, Z.; Liu, V.; Pestourie, R.; Johnson, S. G. Topology optimization of freeform large-area metasurfaces. *Opt. Express* **2019**, *27*, 15765–15775.
- (30) Sell, D.; Yang, J.; Doshay, S.; Fan, J. A. Periodic Dielectric Metasurfaces with High-Efficiency, Multiwavelength Functionalities. *Adv. Opt. Mater.* **2017**, *5*, 1700645.
- (31) Pestourie, R.; Pérez-Arancibia, C.; Lin, Z.; Shin, W.; Capasso, F.; Johnson, S. G. Inverse design of large-area metasurfaces. *Opt. Express* **2018**, *26*, 33732–33747.
- (32) Huang, Y.-W.; Lee, H. W. H.; Sokhoyan, R.; Pala, R. A.; Thyagarajan, K.; Han, S.; Tsai, D. P.; Atwater, H. A. Gate-tunable conducting oxide metasurfaces. *Nano Lett.* **2016**, *16*, 5319–5325.
- (33) Yao, Y.; Shankar, R.; Kats, M. A.; Song, Y.; Kong, J.; Loncar, M.; Capasso, F. Electrically tunable metasurface perfect absorbers for ultrathin mid-infrared optical modulators. *Nano Lett.* **2014**, *14*, 6526–6532.
- (34) Sautter, J.; Staude, I.; Decker, M.; Rusak, E.; Neshev, D. N.; Brener, I.; Kivshar, Y. S. Active tuning of all-dielectric metasurfaces. *ACS Nano* **2015**, *9*, 4308–4315.
- (35) Holsteen, A. L.; Cihan, A. F.; Brongersma, M. L. Temporal color mixing and dynamic beam shaping with silicon metasurfaces. *Science* **2019**, *365*, 257–260.
- (36) Ee, H.-S.; Agarwal, R. Tunable metasurface and flat optical zoom lens on a stretchable substrate. *Nano Lett.* **2016**, *16*, 2818–2823.
- (37) Komar, A.; Paniagua-Domínguez, R.; Miroshnichenko, A.; Yu, Y. F.; Kivshar, Y. S.; Kuznetsov, A. I.; Neshev, D. Dynamic beam switching by liquid crystal tunable dielectric metasurfaces. *ACS Photonics* **2018**, *5*, 1742–1748.
- (38) Savo, S.; Shrekenhamer, D.; Padilla, W. J. Liquid crystal metamaterial absorber spatial light modulator for THz applications. *Adv. Opt. Mater.* **2014**, *2*, 275–279.
- (39) Lee, J.; Jung, S.; Chen, P.-Y.; Lu, F.; Demmerle, F.; Boehm, G.; Amann, M.-C.; Alù, A.; Belkin, M. A. Ultrafast electrically tunable polaritonic metasurfaces. *Adv. Opt. Mater.* **2014**, *2*, 1057–1063.
- (40) Komar, A.; Fang, Z.; Bohn, J.; Sautter, J.; Decker, M.; Miroshnichenko, A.; Pertsch, T.; Brener, I.; Kivshar, Y. S.; Staude, I.; et al. Electrically tunable all-dielectric optical metasurfaces based on liquid crystals. *Appl. Phys. Lett.* **2017**, *110*, No. 071109.
- (41) Shaltout, A. M.; Lagoudakis, K. G.; van de Groep, J.; Kim, S. J.; Vučković, J.; Shalae, V. M.; Brongersma, M. L. Spatiotemporal light control with frequency-gradient metasurfaces. *Science* **2019**, *365*, 374–377.
- (42) Bohn, J.; Bucher, T.; Chong, K. E.; Komar, A.; Choi, D.-Y.; Neshev, D. N.; Kivshar, Y. S.; Pertsch, T.; Staude, I. Active tuning of spontaneous emission by Mie-resonant dielectric metasurfaces. *Nano Lett.* **2018**, *18*, 3461–3465.
- (43) Buchnev, O.; Podoliak, N.; Kaczmarek, M.; Zheludev, N. I.; Fedotov, V. A. Electrically controlled nanostructured metasurface loaded with liquid crystal: toward multifunctional photonic switch. *Adv. Opt. Mater.* **2015**, *3*, 674–679.
- (44) Bendsoe, M. P. *Encyclopedia of Optimization*; Springer, 2001; pp 2636–2638.
- (45) Frandsen, L. H.; Elesin, Y.; Frelsen, L. F.; Mitrovic, M.; Ding, Y.; Sigmund, O.; Yvind, K. Topology optimized mode conversion in a

photonic crystal waveguide fabricated in silicon-on-insulator material. *Opt. Express* **2014**, *22*, 8525–8532.

(46) Su, L.; Piggott, A. Y.; Sapra, N. V.; Petykiewicz, J.; Vuckovic, J. Inverse design and demonstration of a compact on-chip narrowband three-channel wavelength demultiplexer. *ACS Photonics* **2018**, *5*, 301–305.

(47) Sell, D.; Yang, J.; Doshay, S.; Yang, R.; Fan, J. A. Large-angle, multifunctional metagratings based on freeform multimode geometries. *Nano Lett.* **2017**, *17*, 3752–3757.

(48) Callewaert, F.; Velev, V.; Kumar, P.; Sahakian, A.; Aydin, K. Inverse-Designed Broadband All-Dielectric Electromagnetic Metadevices. *Sci. Rep.* **2018**, *8*, 1358.

(49) Ganapati, V.; Miller, O. D.; Yablonovitch, E. Light trapping textures designed by electromagnetic optimization for subwavelength thick solar cells. *IEEE Journal of Photovoltaics* **2014**, *4*, 175–182.

(50) Phan, T.; Sell, D.; Wang, E. W.; Doshay, S.; Edee, K.; Yang, J.; Fan, J. A. High-efficiency, large-area, topology-optimized metasurfaces. *Light: Sci. Appl.* **2019**, *8*, 1–9.

(51) Hughes, T. W.; Minkov, M.; Williamson, I. A.; Fan, S. Adjoint method and inverse design for nonlinear nanophotonic devices. *ACS Photonics* **2018**, *5*, 4781–4787.

(52) Bayati, E.; Pestourie, R.; Colburn, S.; Lin, Z.; Johnson, S. G.; Majumdar, A. Inverse designed metalenses with extended depth of focus. *ACS Photonics* **2020**, *7*, 873–878.

(53) Kafaie Shirmanesh, G.; Sokhoyan, R.; Wu, P. C.; Atwater, H. A. Electro-Optically Tunable Multifunctional Metasurfaces. *ACS Nano* **2020**, *14*, 6912–6920.

(54) Colburn, S.; Zhan, A.; Majumdar, A. Tunable metasurfaces via subwavelength phase shifters with uniform amplitude. *Sci. Rep.* **2017**, *7*, 40174.

(55) Werbos, P. J. *The Roots of Backpropagation*; John Wiley & Sons, Inc., 1994.

(56) Rumelhart, D. E.; Hinton, G. E.; Williams, R. J. Learning representations by back-propagating errors. *Nature* **1986**, *323*, 533–536.

(57) LeCun, Y.; Boser, B.; Denker, J. S.; Henderson, D.; Howard, R. E.; Hubbard, W.; Jackel, L. D. Backpropagation applied to handwritten zip code recognition. *Neural Comput.* **1989**, *1*, 541–551.

(58) Robinson, J.; Rahmat-Samii, Y. Particle swarm optimization in electromagnetics. *IEEE Trans. Antennas Propag.* **2004**, *52*, 397–407.

(59) Jin, N.; Rahmat-Samii, Y. Parallel particle swarm optimization and finite-difference time-domain (PSO/FDTD) algorithm for multi-band and wide-band patch antenna designs. *IEEE Trans. Antennas Propag.* **2005**, *53*, 3459–3468.

(60) Yang, C.-S.; Lin, C.-J.; Pan, R.-P.; Que, C. T.; Yamamoto, K.; Tani, M.; Pan, C.-L. The complex refractive indices of the liquid crystal mixture E7 in the terahertz frequency range. *J. Opt. Soc. Am. B* **2010**, *27*, 1866–1873.

(61) Palik, E. D. *Handbook of Optical Constants of Solids*; Academic Press, 1998; Vol. 3.

(62) Laux, S.; Kaiser, N.; Zöllner, A.; Götzelmann, R.; Lauth, H.; Bernitzki, H. Room-temperature deposition of indium tin oxide thin films with plasma ion-assisted evaporation. *Thin Solid Films* **1998**, *335*, 1–5.

(63) Ma, Z.; Meng, X.; Liu, X.; Si, G.; Liu, Y. Liquid crystal enabled dynamic nanodevices. *Nanomaterials* **2018**, *8*, 871.

(64) Choy, T. C. *Effective Medium Theory: Principles and Applications*; Oxford University Press, 2015; Vol. 165.

(65) Gordon, R. Three sum rules for total optical absorption cross sections. *J. Chem. Phys.* **1963**, *38*, 1724–1729.

(66) Purcell, E. On the absorption and emission of light by interstellar grains. *Astrophys. J.* **1969**, *158*, 433.

(67) Sohl, C.; Gustafsson, M.; Kristensson, G. Physical limitations on broadband scattering by heterogeneous obstacles. *J. Phys. A: Math. Theor.* **2007**, *40*, 11165.

(68) Sanders, S.; Manjavacas, A. Analysis of the Limits of the Local Density of Photonic States near Nanostructures. *ACS Photonics* **2018**, *5*, 2437–2445.

(69) Shim, H.; Fan, L.; Johnson, S. G.; Miller, O. D. Fundamental Limits to Near-Field Optical Response over Any Bandwidth. *Phys. Rev. X* **2019**, *9*, No. 011043.

(70) Kwon, D.-H.; Pozar, D. M. Optimal characteristics of an arbitrary receive antenna. *IEEE Trans. Antennas Propag.* **2009**, *57*, 3720–3727.

(71) Liberal, I.; Ederri, I.; Gonzalo, R.; Ziolkowski, R. W. Upper bounds on scattering processes and metamaterial-inspired structures that reach them. *IEEE Trans. Antennas Propag.* **2014**, *62*, 6344–6353.

(72) Miller, O. D.; Polimeridis, A. G.; Reid, M. T. H.; Hsu, C. W.; DeLacy, B. G.; Joannopoulos, J. D.; Soljačić, M.; Johnson, S. G. Fundamental limits to optical response in absorptive systems. *Opt. Express* **2016**, *24*, 3329–3364.

(73) Zhang, H.; Hsu, C. W.; Miller, O. D. Scattering concentration bounds: brightness theorems for waves. *Optica* **2019**, *6*, 1321–1327.

(74) Angeris, G.; Vuckovic, J.; Boyd, S. P. Computational bounds for photonic design. *ACS Photonics* **2019**, *6*, 1232–1239.

# Supplementary Materials: Tunable metasurface inverse design for 80% switching efficiencies and 144° angular deflection

Haejun Chung<sup>1</sup> and Owen D. Miller<sup>1</sup>

<sup>1</sup>*Department of Applied Physics and Energy Sciences Institute,  
Yale University, New Haven, Connecticut 06511, USA*

(Dated: July 1, 2020)

## CONTENTS

I. Optimized single and triple grating metasurfaces.	1
II. Inverse design framework	4
III. Misalignment tolerance	5
IV. Robustness study	6
V. Mesh convergence study	7
VI. Penalization function	8
VII. Feature size of the optimized gratings	8
VIII. Optimization with $\lambda/10$ feature size for a potential extension to a visible spectrum	9
IX. Geometry parameters	10

### I. OPTIMIZED SINGLE AND TRIPLE GRATING METASURFACES.

We demonstrated high-efficiency single grating to triple grating metasurfaces in Fig. 1 of the main text. Here, we attached detailed optimized structure and diffraction efficiencies. Figure 1 shows single grating metasurfaces for beam deflection ranging from 48° to 120°. The above figures show the optimized structures while the bottom figures are diffraction efficiency at the target wavelength (1550 nm).

Figure 2 shows triple grating metasurfaces for beam deflection ranging from 48° to 120°. The propagation modes are -1, 0, 1 orders here due to the relatively short periodicities. Above figures are the optimized triple grating structures while the bottom figures are corresponding diffraction efficiency figures in broadband. The diffraction efficiencies at the target wavelength show much higher than single grating cases with almost negligible unwanted diffraction modes. Figure 3 shows second order optimization results where the device periods are twice longer than the first order optimized devices. The second order optimized metasurfaces show slight higher efficiencies than the first order optimized metasurfaces. This could be mainly due to the increased degree of freedom in a wider device.

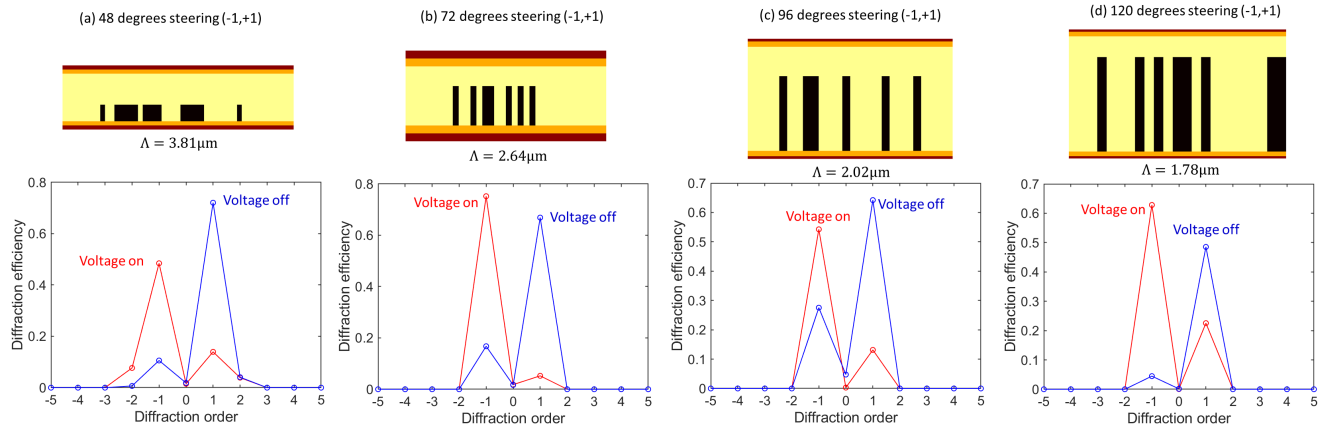


FIG. 1: Optimized single grating metasurfaces for (a) 48° (b) 72° (c) 96° (d) 120° beam deflection.

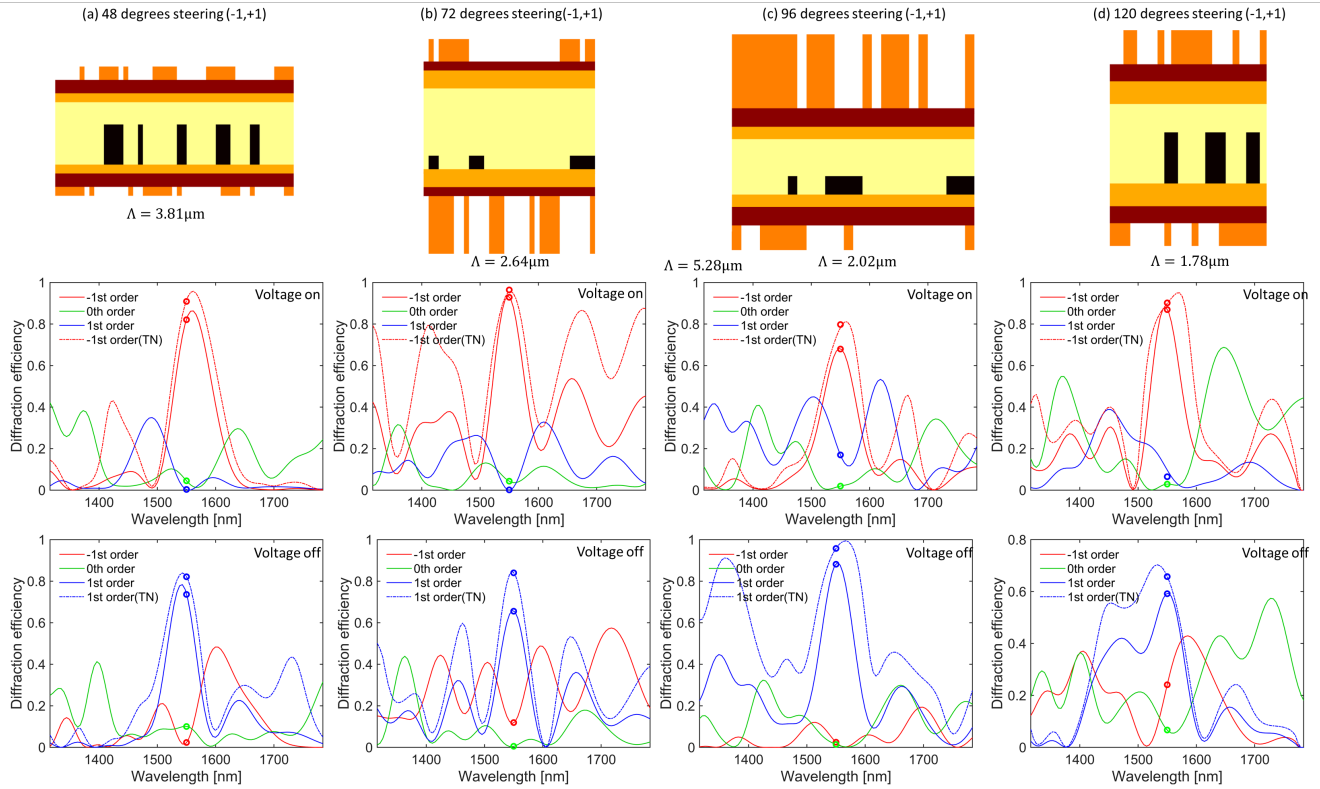


FIG. 2: Optimized triple grating (-1, +1) metasurfaces for (a) 48° (b) 72° (c) 96° (d) 120° beam deflection.

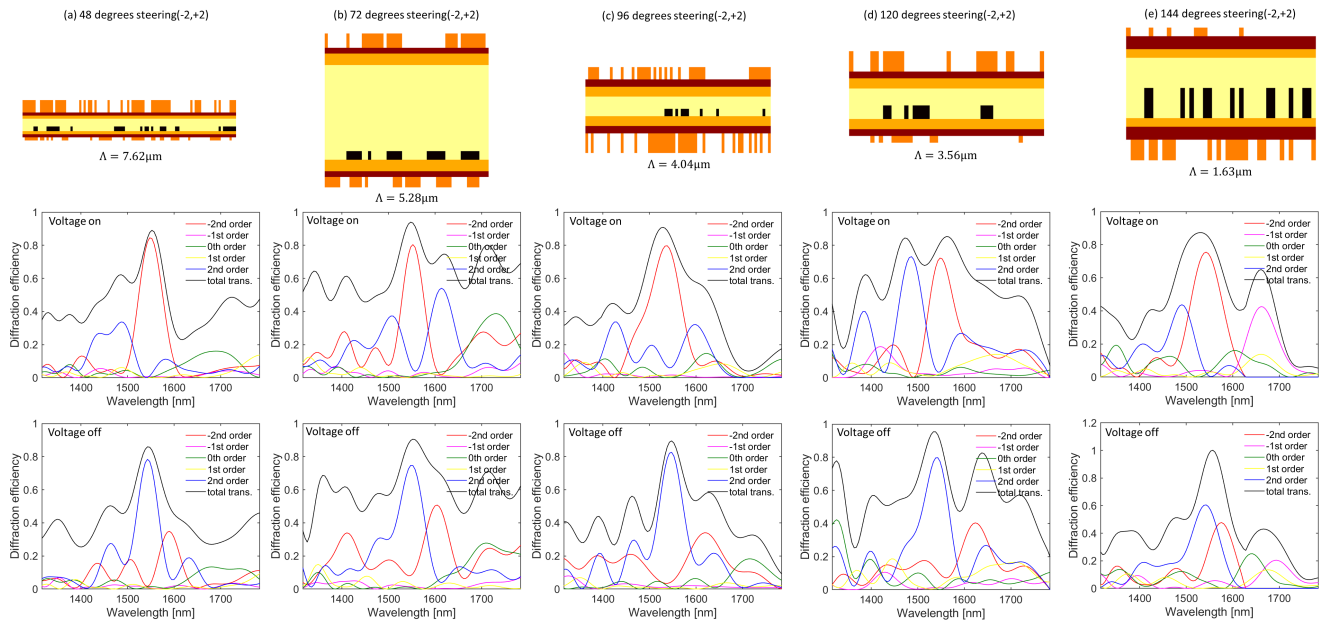


FIG. 3: Optimized triple grating (-2, +2) metasurfaces for (a) 48° (b) 72° (c) 96° (d) 120° beam deflection.

## II. INVERSE DESIGN FRAMEWORK

Consider E-field at the transmission side of the periodic unit:

$$\mathbf{E}(\mathbf{x}) = \frac{1}{A} \sum_n c_n \hat{\mathbf{e}}_n e^{i\mathbf{k}_n \cdot \mathbf{x}} = \sum_n c_n \mathbf{E}_n(\mathbf{x}), \quad (1)$$

where  $\mathbf{k}_n$  the wavevector of each plane wave,  $n$  is a discretized order comprising angle and polarization,  $\hat{\mathbf{e}}_n$  is the polarization unit-vector, and  $c_n$  is  $n_{\text{th}}$  order field coefficient. Then, the diffraction power at  $n_{\text{th}}$  order is defined as

$$P_n = \frac{A}{2Z_0} |c_n|^2 \operatorname{Re} \left( \frac{k_{nz}}{k_0} \right), \quad (2)$$

where  $Z_0$  is a freespace impedance,  $A$  is the area of the periodic unit,  $k_{nz}$  is wave number for  $n_{\text{th}}$  order plane-wave ( $k_{nz} = k_z + n \frac{2\pi}{\Lambda_x}$ ).  $k_{nz}$  will be purely imaginary for evanescent orders, such that  $\operatorname{Re}(k_{nz}) = 0$  for these orders. Note that the incident intensity is given by  $I_{\text{inc}} = \frac{|\mathbf{E}_{\text{inc}}|^2}{2Z_0}$ . Taking  $\mathbf{E}_{\text{inc}} = 1$ , the incident power is  $P_{\text{inc}} = \frac{A}{2Z_0}$ . Thus the transmission is  $T = \frac{P_{\text{trans}}}{P_{\text{inc}}} = \sum_n |c_n|^2 \operatorname{Re}(k_{nz})$ . Then, we define our figure of merit:

$$\mathcal{F} = \frac{1}{T} \left\{ \frac{1}{2} \sum_{s=\text{on,off}} \left[ P_{\text{tar}}^s(\omega, g) - \sum_{j \neq \text{tar}} P_j^s(\omega, g) \right] \right\}, \quad (3)$$

where  $s$  means the state of liquid crystal,  $P_{\text{tar}}^s$  means a target diffraction power,  $P_j^s$  means  $j_{\text{th}}$  order diffraction, and  $T$  is total transmitted power. Then, the current sources for the adjoint simulation can be calculated by  $\mathbf{J}_{\text{adj}} = -i\omega \mathbf{P}_{\text{adj}} = -i\omega \partial \mathcal{F} / \partial \mathbf{E}$ , which can be simplified to:

$$\begin{aligned} \mathbf{J}_{\text{adj}}(\mathbf{x}) &= -i\omega \frac{\partial \mathcal{F}}{\partial \mathbf{E}} \\ &= -\frac{i\omega}{2} [c_{\text{tar}} \cos \theta_{\text{tar}} \mathbf{E}_{\text{tar}}^*(\mathbf{x}) - \sum_{n \neq \text{tar}} c_n \cos \theta_n \mathbf{E}_n^*(\mathbf{x})]. \end{aligned} \quad (4)$$

Once the adjoint fields are computed, the  $\frac{\partial \mathcal{F}}{\partial \varepsilon(\mathbf{x})}$  can be calculated from  $\operatorname{Re}[\mathbf{E}(\mathbf{x}) \cdot \mathbf{E}_{\text{adj}}(\mathbf{x})]$ . The derivatives of  $\mathcal{F}$  with respect to permittivity perturbations can be used for updating the geometry parameters with optimization algorithms including gradient descent or others.

### III. MISALIGNMENT TOLERANCE

To check the efficiency loss due to misalignment, we intentionally moved one of the grating layers as shown in Fig. 4. The misalignment less than the size of one pixel (77.5 nm), we have modified epsilon values of the grating to mimic it which is widely used in the FDTD method. Figure 4 shows that the switching efficiency drop within  $0.03\lambda$

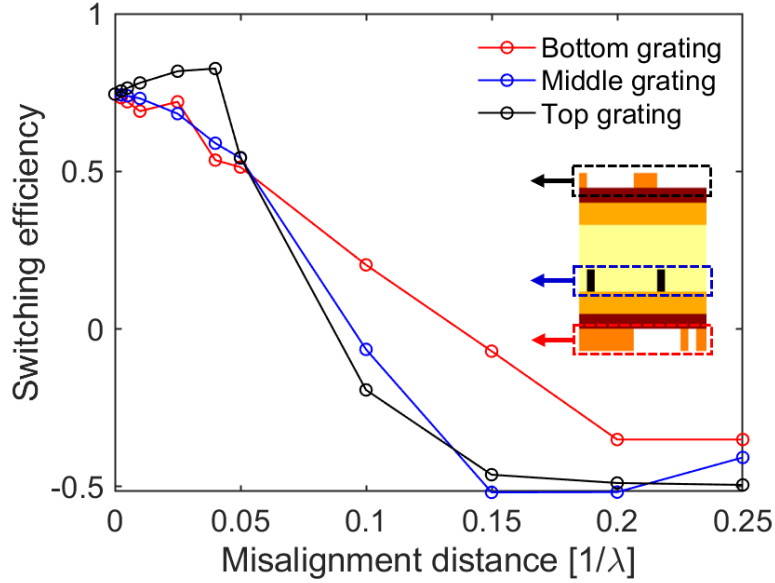


FIG. 4: Switching efficiency loss due to a misalignment of the triple grating. It does not have significant loss within  $0.03\lambda$  (46.5 nm at 1,550 nm wavelength) misalignment.

misalignment (46.5 nm at 1,550 nm wavelength) was less than 7% while the efficiency drops nearly quadratic after  $0.05\lambda$  (77.5 nm at 1,550 nm wavelength).

## IV. ROBUSTNESS STUDY

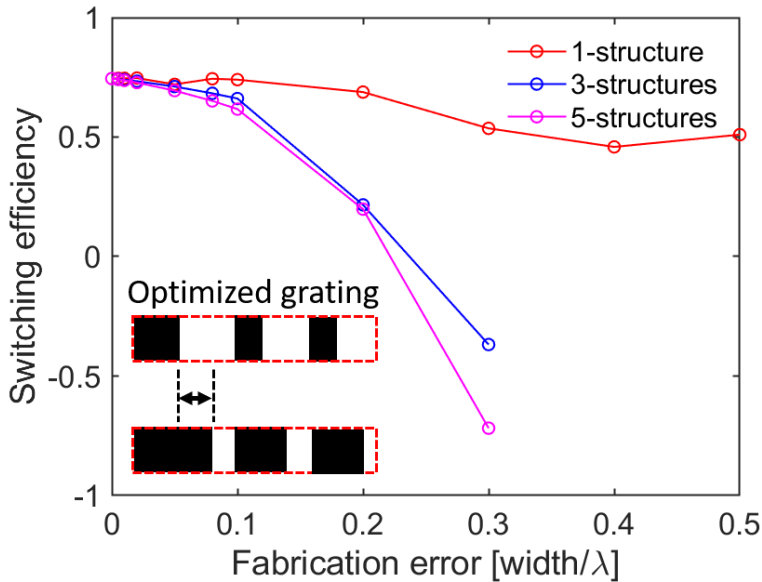


FIG. 5: Robustness test with a varying width of a randomly chosen grating structure in the optimized triple grating. High efficiencies are maintained within  $0.1\lambda$  (155 nm) fabrication errors, and even with much larger errors rather good efficiency is maintained. The inset shows a schematic example of a fabrication error of three randomly chosen grating structures.

The robustness of the optimized metasurfaces was tested by adding / removing nanostructures. First, we randomly picked one nanostructure in the triple grating metasurface in Fig. 5. Then, we varied the width of nano-grating as shown in Fig. 5. Again, the effect of having an error on the width of the grating was negligible within  $0.1\lambda$  size (155 nm at 1,550 nm wavelength) while the efficiency drops faster over  $0.1\lambda$  size error.

## V. MESH CONVERGENCE STUDY

We provide a validation of mesh-size convergence study here. As shown in Fig. 6, the diffraction efficiencies converge well with smaller mesh-size.

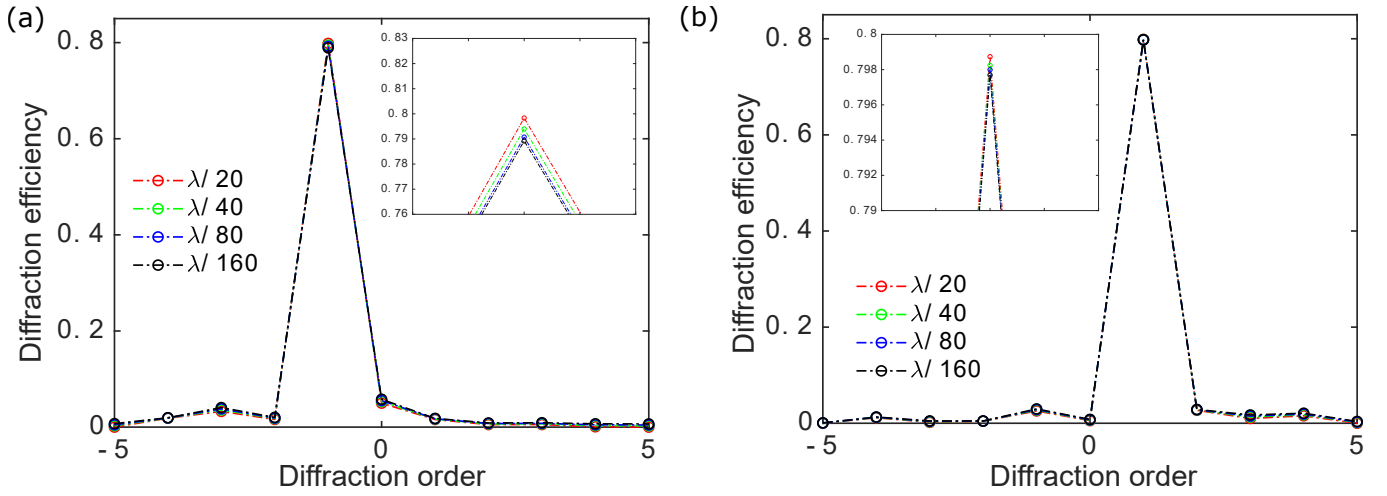


FIG. 6: Validation of mesh-size accuracy for the triple grating structure. The optimization has been done with  $\lambda/20$  mesh-size. Then, we validated it with mesh-sizes of  $\lambda/40$ ,  $\lambda/80$ , and  $\lambda/160$ . (a) voltage on, (b) voltage off.

## VI. PENALIZATION FUNCTION

The penalty function at a position  $x$  in the designable region can be described:

$$P(x) = \zeta \alpha(x) [1 - \alpha(x)] \left[ \frac{\int_{\Omega} \frac{\partial F}{\partial \varepsilon(x)} dx}{V_{\Omega}} \right] \quad (5)$$

where  $\alpha$  is the density of liquid crystal (E7) which varies between 0 and 1 at every point in the structure,  $V_{\Omega}$  means a total volume of the designable region, and  $\zeta$  means a positive weighting function that linearly increases over inverse design iteration.

## VII. FEATURE SIZE OF THE OPTIMIZED GRATINGS

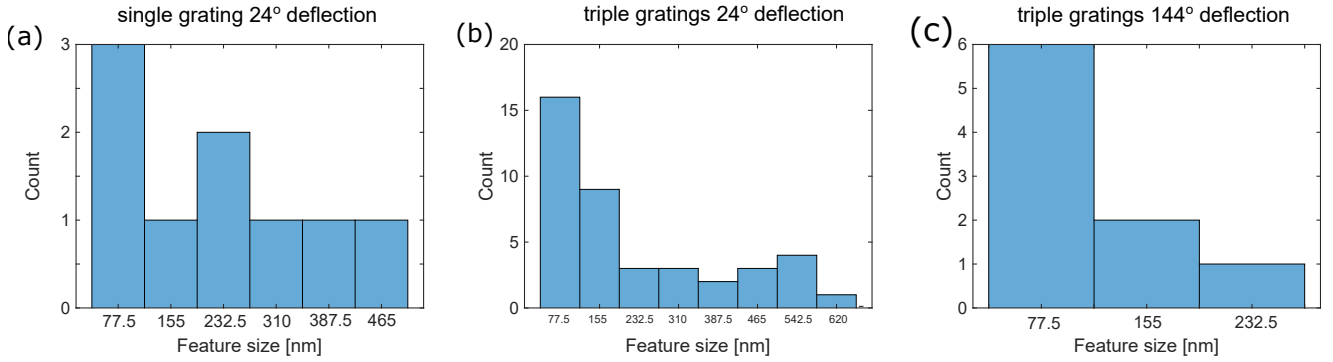


FIG. 7: Histogram of different feature sizes in the optimized gratings. Feature size means the width of the grating structures.

### VIII. OPTIMIZATION WITH $\lambda/10$ FEATURE SIZE FOR A POTENTIAL EXTENSION TO A VISIBLE SPECTRUM

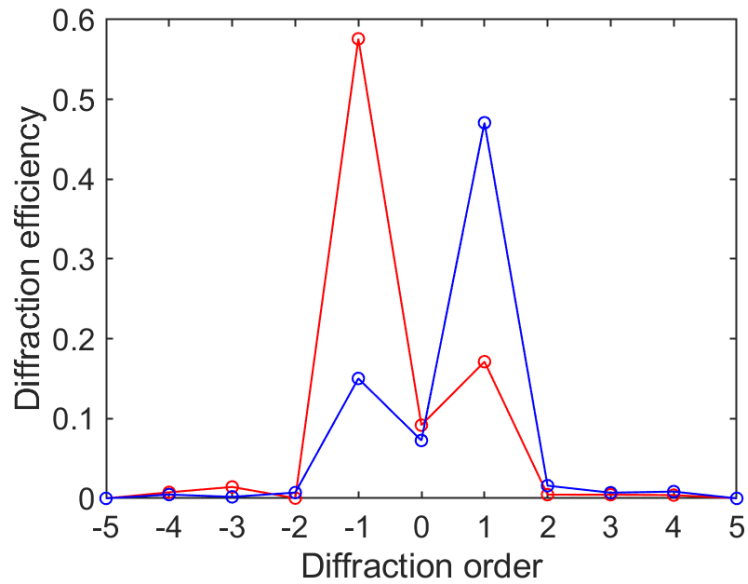


FIG. 8: Diffraction efficiencies of the optimized triple grating structure for 24° beam deflection. 155nm minimum-feature size was used.

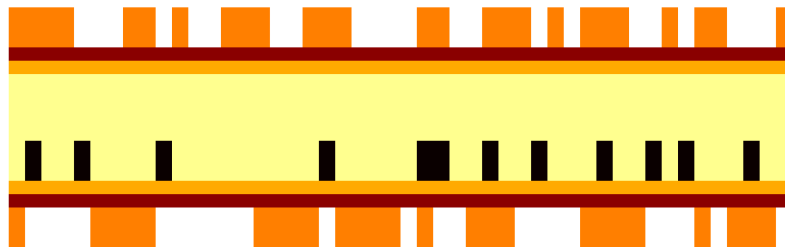


FIG. 9: The optimized triple grating structure for 24° beam deflection with 155nm pixel size.

## IX. GEOMETRY PARAMETERS

TABLE I: Thickness parameters for single-grating metasurfaces. The unit length (a) is 1550 nm. The outer loop of the global optimization determined these parameters.

Layer label	24°	48°	72°	96°	120°
ITO thickness (a)	0.025	0.025	0.050	0.050	0.050
Alignment thickness (a)	0.025	0.025	0.025	0.025	0.075
Si grating thickness (a)	1.000	0.675	0.225	0.175	0.150
bulk LC thickness (a)	0.200	0.250	0.100	0.350	0.100

TABLE II: Grating parameters for single-grating (-1, +1) metasurfaces. Each grid occupies  $0.025a$  length and the height given by Table I. The unit length ( $a$ ) is 1550 nm. The value “1” means epsilon of silicon at 1550 nm, which is 12.11, while the value “0” means epsilon of E7 at 1550 nm which is 2.265 for voltage-on state and 2.877 for voltage-off state.

Grid number	24°	48°	72°	96°	120°	Grid number	24°	48°	72°	96°	120°
1	0	0	0	0	0	50				0	1
2	0	0	0	0	0	51					1
3	0	0	0	0	1	52					1
4	1	0	0	0	0	53					1
5	0	1	0	0	0	54					0
6	0	0	0	0	0	55					1
7	0	0	0	0	0	56					1
8	1	1	0	0	0	57					1
9	0	1	1	1	0	58					1
10	1	0	0	0	0	59					0
11	0	0	0	0	0	60					0
12	1	0	1	1	0	61					0
13	1	1	0	1	0	62					0
14	0	0	1	1	0	63					0
15	1	0	1	1	1	64					0
16	0	0	0	1	0	65					0
17	0	0	0	0	0	66					1
18	0	1	1	1	0	67					1
19	0	0	0	1	0	68					1
20	0	0	1	1	0	69					0
21	0	0	0	1	0	70					0
22	1	1	1	0	0	71					0
23	1	0	0	0	0	72					0
24	0	0	0	0	0	73					0
25		0	0	0	1	74					0
26		0	0	1	1	75					0
27		0	0	1	1	76					0
28			0	1	0	77					0
29			0	1	0	78					0
30			0	1	0	79					0
31			0	0	0	80					0
32			0	0	0	81					0
33			0	0	0	82					0
34			0	0	1	83					0
35			0	0	0	84					0
36				0	1	85					0
37				0	1	86					0
38				1	0	87					0
39				0	0	88					0
40				0	1	89					0
41				0	1	90					0
42				0	1	91					0
43				0	1	92					0
44				0	1	93					0
45				0	1	94					0
46				0	0	95					0
47				0	0	96					0
48				0	0	97					0
49				0	1						

TABLE III: Thickness parameters for triple-grating (-1, +1) metasurfaces. The unit length (a) is 1550 nm. The outer loop of the global optimization determined these parameters.

Layer label	24°	48°	72°	96°	120°	144°
Bottom TiO <sub>2</sub> grating (a)	0.050	0.100	0.100	0.325	0.075	0.075
ITO thickness (a)	0.050	0.050	0.050	0.025	0.050	0.025
Alignment thickness (a)	0.025	0.075	0.025	0.075	0.050	0.050
Si grating thickness (a)	0.200	0.200	0.050	0.050	0.050	0.050
bulk LC thickness (a)	0.100	0.100	0.125	0.350	0.100	0.125
Top TiO <sub>2</sub> grating (a)	0.075	0.150	0.300	0.125	0.075	0.050

TABLE IV: Grating parameters for the bottom  $\text{TiO}_2$  grating of the triple-grating (-1, +1) metasurfaces. Each grid occupies  $0.025a$  length and the height given by Table III. The unit length ( $a$ ) is 1550 nm. The value “1” means epsilon of  $\text{TiO}_2$  at 1550 nm, which is 6.027, while the value “0” means freespace.

Grid number	24°	48°	72°	96°	120°	144°	Grid number	24°	48°	72°	96°	120°	144°
1	0	1	1	0	1	1	50					1	1
2	0	1	0	1	1	1	51						1
3	0	1	0	1	1	1	52						0
4	1	0	1	1	1	1	53						1
5	0	0	1	1	1	1	54						0
6	0	0	1	1	1	1	55						0
7	1	0	1	0	0	1	56						0
8	1	0	1	0	1	0	57						0
9	0	1	0	1	0	0	58						1
10	1	0	0	0	0	0	59						1
11	0	0	0	0	0	0	60						0
12	0	0	0	0	0	0	61						1
13	0	1	1	0	0	0	62						1
14	0	0	0	1	0	1	63						1
15	0	0	0	1	0	0	64						1
16	0	0	0	1	1	1	65						1
17	1	1	0	0	0	1	66						1
18	0	1	0	0	0	1	67						1
19	0	1	0	0	1	1	68						0
20	0	1	0	0	1	1	69						0
21	0	1	0	0	1	1	70						1
22	0	1	0	1	1	0	71						0
23		1	0	0	1	1	72						1
24		1	0	1	1	1	73						0
25			0	1	0	0	74						1
26			1	1	1	0	75						1
27			0	1	0	0	76						1
28				0	0	0	77						1
29				0	0	0	78						1
30				0	0	1	79						1
31				0	0	1	80						0
32				0	0	1	81						1
33				0	0	1	82						1
34				1	0	1	83						0
35				0	1	1	84						1
36					1	1	85						1
37					1	0	86						1
38					1	0	87						1
39					0	1	88						1
40					0	0	89						1
41					1	0	90						1
42					0	0	91						0
43					0	0	92						0
44					0	1	93						0
45					0	1	94						0
46					0	1	95						0
47					0	1	96						1
48					1	1	97						0
49					1	1							

TABLE V: Grating parameters of the silicon grating in triple-grating (-1, +1) metasurfaces. Each grid occupies  $0.025a$  length and the height given by Table III. The unit length ( $a$ ) is 1550 nm. The value “1” means epsilon of silicon at 1550 nm, which is 12.11, while the value “0” means epsilon of E7 at 1550 nm which is 2.265 for voltage-on state and 2.877 for voltage-off state.

Grid number	24°	48°	72°	96°	120°	144°	Grid number	24°	48°	72°	96°	120°	144°
1	0	0	0	0	0	0	50					0	0
2	1	0	0	1	0	1	51						0
3	1	0	0	1	0	0	52						1
4	0	0	0	0	0	0	53						1
5	1	0	0	0	0	0	54						0
6	0	0	0	0	0	0	55						0
7	0	0	1	0	0	0	56						0
8	0	0	0	0	0	0	57						0
9	0	1	0	0	0	0	58						1
10	0	1	0	1	0	0	59						1
11	0	0	1	1	1	1	60						1
12	0	0	1	1	1	0	61						0
13	0	0	1	0	1	0	62						0
14	0	0	1	0	1	0	63						0
15	0	1	0	0	0	0	64						0
16	0	1	0	0	0	0	65						1
17	0	1	0	0	0	0	66						1
18	1	0	0	0	1	0	67						0
19	1	0	0	0	0	0	68						0
20	1	0	0	0	0	0	69						0
21	0	1	0	0	0	0	70						0
22	0	1	0	0	0	0	71						0
23	0	0	0	0	0	0	72						0
24	0	1	0	0	0	0	73						0
25		1	0	0	0	0	74						0
26			1	0	1	0	75						0
27			0	0	1	0	76						0
28				0	0	0	77						0
29				0	0	0	78						0
30				1	0	0	79						0
31				1	0	0	80						0
32				1	0	0	81						1
33				1	0	0	82						1
34				1	1	1	83						0
35				0	1	0	84						0
36					1	0	85						0
37					0	0	86						0
38					0	0	87						0
39					0	0	88						0
40					0	0	89						0
41					1	0	90						0
42					1	0	91						0
43					0	0	92						0
44					0	0	93						1
45					0	0	94						1
46					0	1	95						0
47					0	1	96						0
48					0	1	97						0
49					0	0							

TABLE VI: Grating parameters of the top  $\text{TiO}_2$  grating in triple-grating (-1, +1) metasurfaces. Each grid occupies  $0.025a$  length and the height given by Table III. The unit length ( $a$ ) is  $1550 \text{ nm}$ . The value “1” means epsilon of  $\text{TiO}_2$  at  $1550 \text{ nm}$ , which is  $6.027$ , while the value “0” means freespace.

Grid number	24°	48°	72°	96°	120°	144°	Grid number	24°	48°	72°	96°	120°	144°
1	0	0	1	0	0	1	50					0	1
2	0	0	1	1	0	0	51						1
3	0	1	1	0	0	0	52						1
4	0	1	1	1	0	0	53						1
5	0	0	1	1	0	0	54						1
6	1	0	1	1	1	0	55						0
7	0	0	1	1	0	0	56						0
8	0	1	0	1	0	1	57						0
9	0	0	1	1	0	1	58						0
10	0	1	1	0	1	1	59						1
11	0	1	1	0	1	0	60						1
12	0	1	0	0	1	0	61						0
13	0	1	0	0	1	0	62						0
14	0	1	0	0	0	0	63						1
15	0	1	1	0	1	0	64						1
16	1	0	0	0	0	0	65						1
17	0	0	1	0	0	0	66						1
18	0	0	1	0	0	0	67						1
19	0	1	1	0	0	0	68						0
20	0	0	0	0	0	0	69						0
21	0	0	1	0	1	1	70						0
22	0	0	0	0	1	0	71						0
23		1	0	0	1	1	72						1
24		1	0	0	1	1	73						0
25			0	0	1	1	74						1
26			1	0	0	1	75						0
27			0	0	0	1	76						1
28				1	0	0	77						1
29				1	0	0	78						1
30				1	0	0	79						1
31				1	0	1	80						0
32				0	1	1	81						0
33				1	1	0	82						0
34				1	1	0	83						0
35				1	1	0	84						0
36					1	0	85						0
37					1	0	86						1
38					0	1	87						0
39					0	1	88						0
40					0	1	89						0
41					0	1	90						1
42					0	0	91						1
43					0	0	92						1
44					0	0	93						1
45					0	0	94						0
46					1	0	95						0
47					1	0	96						0
48					1	0	97						1
49					1	1							

TABLE VII: Thickness parameters for triple-grating (-2, +2) metasurfaces. The unit length (a) is 1550 nm. The outer loop of the global optimization determined these parameters.

Layer label	48°	72°	96°	120°	144°
Bottom TiO <sub>2</sub> grating (a)	0.350	0.050	0.100	0.200	0.050
ITO thickness (a)	0.050	0.025	0.025	0.050	0.025
Alignment thickness (a)	0.025	0.050	0.075	0.075	0.025
Si grating thickness (a)	0.150	0.075	0.050	0.050	0.050
bulk LC thickness (a)	0.150	0.100	0.725	0.100	0.100
Top TiO <sub>2</sub> grating (a)	0.050	0.150	0.125	0.125	0.200

TABLE VIII: Grating parameters of the bottom  $\text{TiO}_2$  grating in triple-grating (-2, +2) metasurfaces. Each grid occupies  $0.025a$  length and the height given by Table VII. The unit length ( $a$ ) is  $1550 \text{ nm}$ . The value “1” means epsilon of  $\text{TiO}_2$  at  $1550 \text{ nm}$ , which is  $6.027$ , while the value “0” means freespace.

Grid number	48°	72°	96°	120°	144°	Grid number	48°	72°	96°	120°	144°
1	0	0	1	1	0	51			0	1	1
2	1	0	1	0	1	52			0	0	1
3	1	0	1	1	1	53			0	0	1
4	1	0	1	0	1	54			0	0	1
5	0	0	1	0	1	55				1	1
6	1	1	0	0	1	56				0	1
7	1	0	0	0	1	57				1	0
8	0	1	0	0	0	58				1	0
9	1	0	1	1	1	59				0	0
10	1	0	1	0	1	60				0	1
11	1	1	1	0	0	61				1	1
12	0	1	1	0	1	62				0	0
13	0	1	0	0	0	63				1	0
14	0	1	1	1	1	64				0	1
15	0	1	0	0	0	65				1	1
16	0	0	0	0	0	66				0	0
17	0	0	0	0	0	67				0	0
18	0	0	0	0	0	68				1	0
19	1	0	0	1	1	69				0	1
20	0	1	0	0	1	70					1
21	1	1	0	0	1	71					1
22	0	0	0	0	0	72					1
23	1	0	1	0	0	73					0
24	1	0	1	1	0	74					0
25	1	0	1	1	0	75					0
26	1	0	0	1	0	76					0
27	1	0	1	1	0	77					1
28	0	0	1	1	0	78					0
29	0	0	1	1	0	79					0
30	1	0	1	1	0	80					0
31	1	0	1	1	0	81					0
32	0	0	0	1	1	82					0
33	0	0	0	1	0	83					0
34	0	0	0	0	0	84					0
35	1	0	0	1	0	85					0
36	0	0	0	1	1	86					0
37	1	0	1	1	1	87					1
38	0	0	1	1	1	88					1
39	0	0	1	1	1	89					1
40	0	0	1	1	1	90					1
41	0	1	1	1	1	91					1
42	1	0	0	0	0	92					0
43	0	0	0	0	0	93					0
44		0	0	1	0	94					0
45		0	0	0	0	95					0
46		0	0	0	0	96					1
47		0	1	0	1	97					0
48			1	0	0	98					0
49			1	0	0	99					1
50			1	0	0						

TABLE IX: Grating parameters of the silicon grating in triple-grating (-2, +2) metasurfaces. Each grid occupies 0.025a length and the height given by Table VII. The unit length (a) is 1550 nm. The value “1” means epsilon of silicon at 1550 nm while the value “0” means epsilon of E7.

Grid number	48°	72°	96°	120°	144°	Grid number	48°	72°	96°	120°	144°
1	0	0	0	0	0	51			0	0	0
2	0	0	0	0	0	52			0	0	0
3	0	0	0	0	0	53			0	0	0
4	0	0	0	0	0	54			0	0	0
5	1	0	0	0	0	55				0	1
6	1	0	0	0	1	56				0	0
7	0	0	0	0	1	57				0	1
8	0	0	1	0	0	58				0	1
9	0	1	1	0	0	59				0	0
10	0	1	1	0	0	60				0	1
11	0	0	1	0	0	61				0	0
12	0	0	1	0	1	62				0	0
13	1	0	0	0	1	63				0	0
14	0	1	0	0	1	64				0	1
15	1	0	1	0	1	65				0	1
16	0	1	0	0	1	66				1	1
17	0	1	0	0	1	67				0	0
18	1	1	0	0	0	68				0	0
19	1	1	0	0	0	69				0	0
20	0	0	0	0	0	70					0
21	0	0	1	0	0	71					1
22	0	0	1	0	0	72					1
23	0	0	1	0	1	73					0
24	1	0	1	0	0	74					0
25	0	0	1	0	0	75					0
26	1	0	0	0	0	76					0
27	0	0	0	0	0	77					0
28	0	0	0	0	0	78					0
29	0	0	0	0	0	79					0
30	0	0	0	1	0	80					0
31	0	0	0	1	0	81					0
32	1	1	0	1	0	82					0
33	1	1	0	0	0	83					0
34	0	1	1	1	0	84					0
35	0	0	1	0	0	85					0
36	0	0	1	1	0	86					0
37	1	0	1	1	0	87					0
38	0	0	1	1	0	88					0
39	0	0	1	0	0	89					0
40	1	0	0	0	0	90					0
41	1	0	0	0	0	91					1
42	0	0	0	0	0	92					0
43	0	0	0	1	1	93					1
44		0	0	0	1	94					1
45		0	1	0	1	95					1
46		0	1	0	1	96					1
47		0	1	0	1	97					1
48			1	0	0	98					1
49			1	1	0	99					0
50			1	0	0						

TABLE X: Grating parameters of the top  $\text{TiO}_2$  grating in triple-grating (-2, +2) metasurfaces. Each grid occupies  $0.025a$  length and the height given by Table VII. The unit length ( $a$ ) is 1550 nm. The value “1” means epsilon of  $\text{TiO}_2$  at 1550 nm, which is 6.027, while the value “0” means freespace.

Grid number	48°	72°	96°	120°	144°	Grid number	48°	72°	96°	120°	144°
1	1	1	1	0	1	51			1	0	1
2	0	0	0	1	1	52			1	0	1
3	0	0	0	1	1	53			0	0	1
4	0	0	0	1	1	54			0	0	1
5	0	0	0	1	1	55				0	1
6	1	1	0	0	1	56				0	1
7	0	1	0	0	0	57				0	0
8	0	0	1	0	0	58				0	0
9	0	1	0	0	1	59				0	0
10	1	1	0	1	1	60				0	1
11	0	1	0	0	1	61				1	1
12	0	1	0	0	1	62				1	1
13	0	1	1	0	1	63				1	1
14	0	0	1	1	1	64				1	1
15	0	0	1	0	0	65				1	1
16	1	0	1	0	1	66				1	1
17	1	0	1	0	1	67				1	1
18	1	0	1	1	1	68				1	1
19	0	0	1	0	1	69				1	0
20	0	0	0	1	1	70					0
21	0	0	1	1	0	71					0
22	0	0	1	1	0	72					0
23	0	0	1	1	0	73					0
24	0	1	1	1	0	74					0
25	0	0	1	0	0	75					0
26	1	0	0	1	0	76					0
27	0	0	0	0	1	77					0
28	0	0	0	1	0	78					1
29	0	0	0	0	1	79					0
30	0	0	0	1	0	80					1
31	0	1	0	0	1	81					1
32	0	1	0	1	1	82					1
33	0	1	0	0	0	83					0
34	0	1	0	0	1	84					0
35	0	1	0	1	0	85					0
36	0	0	0	0	0	86					0
37	0	0	0	0	0	87					0
38	0	1	0	0	0	88					0
39	0	1	0	1	0	89					1
40	0	0	1	1	1	90					0
41	0	0	1	1	0	91					1
42	0	0	1	1	0	92					0
43	0	0	1	1	0	93					0
44		0	0	1	0	94					0
45		0	1	0	0	95					0
46		1	1	0	1	96					1
47		0	1	0	0	97					1
48			1	0	0	98					1
49			1	0	1	99					0
50			1	0	0						